

# Programmable Photonic Microwave Filters Monolithically Integrated in InP–InGaAsP

Erik J. Norberg, Robert S. Guzzon, John S. Parker, Leif A. Johansson, *Member, IEEE*, and Larry A. Coldren, *Fellow, IEEE*

**Abstract**—We demonstrate an integrated programmable photonic filter structure capable of producing bandpass filters with both tunable passband bandwidth and center frequency. Such filters could provide dynamic pre-filtering of very wide bandwidth analog microwave signals, essential to the next generation RF-front ends. The photonic filter is constructed from an array of uncoupled identical filter stages, each reconfigurable as a zero or a pole using an asymmetrical Mach-Zehnder Interferometer (MZI) structure with feedback. Integrated on a standard InP–InGaAsP material platform, semiconductor optical amplifiers (SOAs) and current injected phase modulators (PMs) are used to rapidly adjust the individual pole and zero locations, thereby reconfiguring the overall filter function. In this paper, we demonstrate cascaded filter structures with up to four filter stages, capable of producing a variety of higher order filters. Demonstrated filters have a free spectral range (FSR) of 23.5 or 47 GHz. A center frequency tunability over 28 GHz is demonstrated for a 2nd order bandpass filter, and a passband tunability of 1.9–5.4 GHz with stopband rejection >32 dB using 3rd and 4th order filters. Finally, the linearity of our active filters is investigated; a preliminary spurious-free dynamic range (SFDR) of 86.3 dB·Hz<sup>2/3</sup> is obtained. However, we believe this number can be improved significantly by optimizing the design.

**Index Terms**—Microwave filters, optical filters, optical waveguide components, photonic integrated circuits (PIC), resonators.

## I. INTRODUCTION

**B**OTH for commercial communication and military electronic warfare and radar, there is an ever increasing interest in RF-systems that can handle very wide instantaneous bandwidths as well as high frequency bands. Thus, RF-front ends with instantaneous bandwidths up to 100 GHz might soon be desired [1]. For the signal processing of such ultra-wide bandwidth signals, photonics can find indispensable utility, drawing on the inherent wide bandwidth tunability, low loss, and size, weight and power (SWaP) performance, compared to their electronic counterparts. For example, by rapidly pre-filtering wide bandwidth analog signals in the optical domain the analog-to-digital conversion (ADC) and subsequent digital

signal processing (DSP) can be significantly relieved [2]. Such photonic filters should have a tunable passband and center frequency, to accommodate different channel widths and frequencies, as well as enable tracking and sweeping in the RF domain.

Optical signal processing was proposed almost three decades ago [3], and has been immensely investigated since [2]. However, fiber and bulk optics is inevitably limited by incoherent filtering due to the limited stability against environmental changes. This makes it difficult to achieve negative filter coefficients and the very complex filter characteristics needed for the RF signal processing application. Integrated optics, on the other hand, can provide the stability needed for coherent filtering, and have already demonstrated usefulness as channelizing add/drop filters in wavelength division multiplexing (WDM) applications [4], [5]. Recently, there have also been significant advances in the realization of integrated photonic filters pushing towards the RF domain [1], [6]–[12]. We have previously proposed and demonstrated the basic building block for a cascaded filter structure, that incorporates a resonator and Mach-Zehnder Interferometer (MZI) for reconfigurable filter functions [6]. Similar filter building blocks have in parallel been proposed and demonstrated on other integration platforms including: silicon-on-insulator (SOI) with no optical gain [7], [8] and SOI-IIIIV hybrid [9]. We have also demonstrated the ability to cascade several filter stages to produce higher order filters with tunable filter characteristics [11], [12]. In this paper, we present a deeper investigation and description of our optical filter design, and present more cascaded stages together with improved results on passband bandwidth and center frequency tunability. Additionally, we investigate the linearity performance of our active devices by measuring the spurious-free dynamic range (SFDR).

## II. FILTER DESIGN

### A. Programmable Filter Design

Working within the coherent filter regime, versatile tunable filters can be achieved using a cascaded filter design that incorporates both ring resonators and MZIs, to provide poles and zeros respectively [13]. For such cascaded filters, there are two main design categories, coupled and uncoupled arrays; each approach has its advantages and drawbacks. The main advantage of a coupled resonator arrangement is the enhanced filter roll-off and improved extinction compared to the uncoupled design, resulting from the higher pole magnitudes obtained from the same number of resonators [13]. For the coupled system, the filter passband bandwidth is set by the inter-stage coupling strength.

Manuscript received December 24, 2010; revised March 12, 2011; accepted March 20, 2011. Date of publication March 28, 2011; date of current version May 20, 2011. This work was supported in part by the Defense Advanced Research Projects Agency (DARPA) under the PhASER project. A portion of this work was performed in the UCSB Nanofabrication Facility, part of the NSF funded NNIN network.

The authors are with the Department of Electrical and Computer Engineering, University of California Santa Barbara, Santa Barbara, CA 93106 USA (e-mail: norberg@ece.ucsb.edu).

Color versions of one or more of the figures in this paper are available online at <http://ieeexplore.ieee.org>.

Digital Object Identifier 10.1109/JLT.2011.2134073

This requires tunable couplers, which entails additional control and can be more difficult to implement. On the contrary, for an uncoupled system, the filter shape is independent of coupling strength and the filter synthesis is made very simple through multiplied transfer functions. Although the coupled and uncoupled design is fundamentally different, very comparable filter functions can be achieved, as we have previously demonstrated [10], [11].

In this work, in favor of control and simplicity in filter synthesis, we focus on entirely uncoupled filter arrays. For maximum flexibility in filter synthesis, each filter stage should be designed to be reprogrammable as either a zero or a pole, with arbitrary magnitude and phase. The scattering parameters and magnitude response for the individual filter stage and the overall filter array are then given by:

$$\begin{aligned} |S_{21}^{\text{pole}}|^2 &= \left| \frac{A}{1 - G_p e^{-j\beta L_p}} \right|^2 \\ &= \frac{A^2}{1 - 2G_p \cos[\beta L_p] + G_p^2} \end{aligned} \quad (1)$$

where  $\beta L_p = (2\pi)/(FSR)(f - f_c) + \varphi_p$ , or,

$$\begin{aligned} |S_{21}^{\text{zero}}|^2 &= |B(1 - G_z e^{-j\beta L_z})|^2 \\ &= B^2(1 - 2G_z \cos[\beta L_z] + G_z^2) \end{aligned} \quad (2)$$

with  $\beta L_z = (2\pi)/(FSR)(f - f_c) + \varphi_z$ . (1) and (2) describes the magnitude response of the individual filter stage programmed as either a pole or a zero, respectively.  $G_p$  ( $G_z$ ) denotes the pole (zero) magnitude, and  $\varphi_p$  ( $\varphi_z$ ) the pole or zero phase, while  $f - f_c$  denotes the deviation from some given center frequency  $f_c$ , and FSR denotes the free spectral range of the pole or zero.  $A$  and  $B$  represent the gain or loss that the signal experiences going through each stage, but does not influence the relative filter shape. Given by the uncoupled nature of the structure, (3) shows how the overall magnitude transfer function for a filter array of  $N$  stages results from the product sequence of the individual filter stages ( $j$ ).

$$|S_{21}^{\text{Total}}|^2 = \prod_j |S_{21}^j|^2. \quad (3)$$

Fig. 1 are simulated using (1)–(3), and demonstrates the flexible filter synthesis that can be achieved with a relatively simple filter array. Simulating only four filter stages using only zeros, only poles or a mix of zeros and poles, bandpass and bandstop filter are synthesized. The filter functions are displayed in normalized frequency for ease of comparison, and the programmed pole and zero locations for each filter case are shown in the pole-zero diagrams, inset in Fig. 1. The pole magnitudes were limited to  $<0.9$  for the simulations to be realistic. We experimentally found that for pole values above  $\sim 0.9$  mode competition becomes prominent. In essence, the gain (pole values) start to clamp for the majority of the mode spectrum while only one or a few modes experience higher pole values, i.e., the device approaches lasing.

In the next section, we describe the actual optical filter design, and explain how the pole and zero reconfigurability with

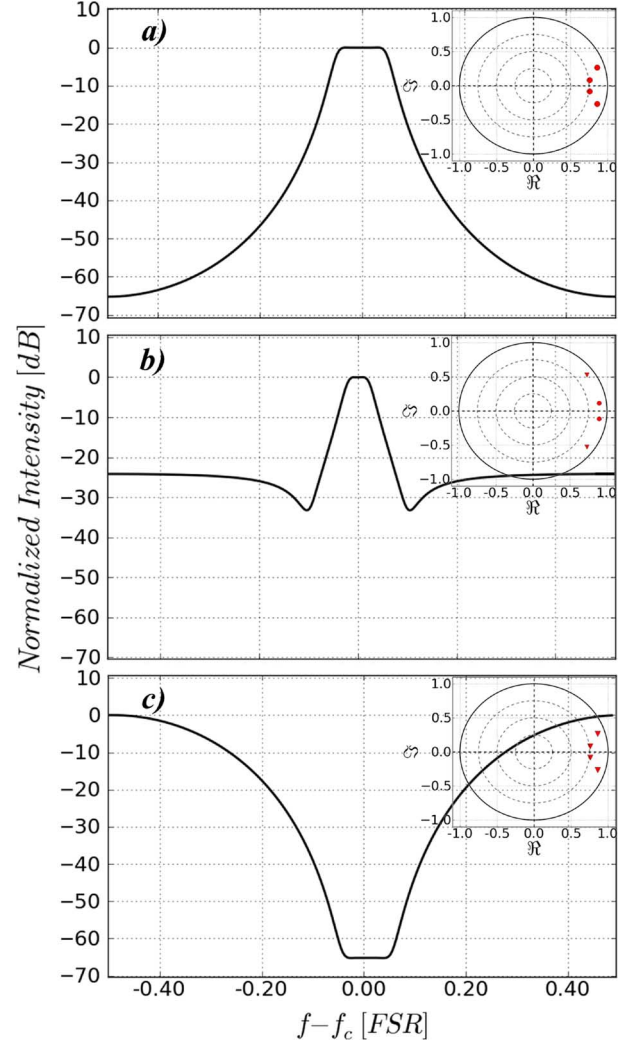


Fig. 1. Simulated 4th order reconfigurable filter responses. (a) Bandpass filter using only poles. (b) Bandpass filter using two poles and two zeros, yielding sharper filter roll-off but poorer stopband rejection. (c) Bandstop filter using only zeros. Inset show pole (circle) and zero (triangle) locations in each case.

arbitrary phase and magnitude are achieved in the single filter stage.

## B. Optical Filter Design

For the coherent filtering in the previous section to be possible, the optical filter design is implemented on a single chip using monolithic integration. Still, in favor of control and stability as well as potential fabrication yield issues, we have in this work limited the filter array to five filter stages. A schematic of the optical filter chip is shown in Fig. 2(a), with the single filter stage highlighted in Fig. 2(b).

The single filter stage in Fig. 2(b) consists of an asymmetrical MZI with a feedback path connecting the output to the input, thus forming two resonator paths with different delay. Therefore, the single filter stage response really consists of two poles and one zero, however, the idea as outlined in the previous section is to utilize either only one pole or one zero per unit cell at any one time. The individual pole or zero is isolated by utilizing active semiconductor optical amplifier (SOA) elements

that provide gain or absorption. These SOAs are used to amplify or turn off different waveguide paths. If one of the lower waveguides is turned off, by reverse biasing SOA<sub>1</sub> ( $G_1 = 0$ ) or SOA<sub>2</sub> ( $G_2 = 0$ ), a single pole response is isolated, as shown in Fig. 2(c), and described by the optical scattering parameters in (4) and (5) respectively. If the top waveguide is turned off instead, a single zero through the remaining MZI path results, this is shown in Fig. 2(c) and described by the scattering parameters in (6). By designing the lengths of the different waveguide paths ( $L_{1,2,3}$ ), desired FSR and filter bandwidths are achieved. In this work, the two resonators have a length of 1.750 or 3.500 mm, corresponding to time delays of 21.5 and 42.5 ps, or FSRs of 47 and 23.5 GHz respectively. The MZI was designed with a path difference of 21.5 ps (FSR of 47 GHz) as well.

$$\begin{aligned} & \left| S_{21}^{\text{pole2}} \right|_{G_1=0}^2 \\ &= \left| \frac{G_{ff} 0.5 \alpha_2 G_2}{1 - 0.5 \alpha_2 \alpha_3 G_2 G_3 e^{-j[\beta(L_2+L_3)+\varphi_2]}} \right|^2 \end{aligned} \quad (4)$$

$$\begin{aligned} & \left| S_{21}^{\text{pole1}} \right|_{G_2=0}^2 \\ &= \left| \frac{G_{ff} 0.5 \alpha_1 G_1}{1 + 0.5 \alpha_1 \alpha_3 G_1 G_3 e^{-j[\beta(L_1+L_3)+\varphi_1]}} \right|^2 \end{aligned} \quad (5)$$

$$\begin{aligned} & \left| S_{21}^{\text{zero}} \right|_{G_3=0}^2 \\ &= (0.5 G_{ff})^2 \left| 1 - \frac{\alpha_2}{\alpha_1} G_1 G_3 e^{-j[\beta(L_2-L_1)+\varphi_2-\varphi_1]} \right|^2. \end{aligned} \quad (6)$$

The optical scattering parameters shown in (4)–(6), includes all optical effects to first order. 0.5 appears in the equation assuming lossless 3 dB couplers throughout,  $L$  and  $\alpha$  is the length and fractional loss of the different waveguide sections,  $G$  and  $\varphi$  represent the gain and phase added from the SOA and phase-modulators (PMs) respectively, and  $\beta$  is the propagation constant of the waveguide. Equation (4) and (5) are analog to (1), and (6) to (2). For example, comparing (6) and (2): it is clear from the phase condition that  $L_z = L_2 - L_1$  and  $\varphi_z = \varphi_2 - \varphi_1$ . While the amplitude transmission gives  $B = 0.5 G_{ff}$  and  $G_z = \alpha_2 / \alpha_1 G_1 G_3$ . Thus, we see that the pole and zero locations governed by  $G$  and  $\varphi$  in (1) and (2) are in the optical filter design simply controlled by adjusting the gain of the SOAs and phase of the phase modulators, since the waveguide losses and coupling ratios are fixed. We will for the sake of conciseness, in this paper, refer to  $G$  and  $\varphi$  in (1) and (2) when analyzing our measured filter functions. Finally, we note that if no phase ( $\varphi_{2,3} = 0$ ) is applied, there is a  $\pi$  (half FSR) offset between the short and long resonator response, as shown in Fig. 2(c). This is also expressed in (5) compared to (4) with the + instead of in the denominator. For the longer resonator case described in (5), this discrepancy is caused by the  $-\pi/2$  acquired phase from each MMI cross-couplings in one round trip.

### III. DEVICE FABRICATION AND INTEGRATION PLATFORM

In order to utilize on-chip gain and fast phase modulation we have turned to the InP–InGaAsP material system. This mature photonic integration platform has the advantage of efficient

semiconductor amplifiers in the telecom C-band, and efficient and quick phase modulation using current injected phase modulators. The re-programming and tuning time constants of the filter is ultimately limited by the response time of the gain and phase controllers, which here is governed by the carrier lifetime on the ns time scale [14]. This ultimately allows for close to real-time tracking and sweeping in the RF domain, essential for many applications.

For long filter cascades with significant accumulated loss, on-chip gain is also necessary to avoid signal degradation and maintain a reasonable noise figure. However, when utilizing SOAs, careful consideration must be taken to minimizing the added amplifier noise and avoid gain saturation effects. These effects will degrade the noise figure and the third order intercept point (IP3), respectively, and lead to a SFDR. For this reason, we have utilized a high saturation and low gain offset quantum well (QW) integration platform. In this integration scheme, the quantum wells are placed on top of the waveguide for lowered active confinement factor and thus more linear amplifiers [15], compared to centered quantum wells. The SFDR performance of our programmable filters is characterized and discussed in Section IV.E of this paper.

Our programmable photonic filters are monolithically integrated, with all mask steps patterned by standard i-line stepper photolithography. Only a single blanket InP regrowth is needed to provide the p-cladding, after the quantum wells have been selectively removed to create passive waveguide sections. Attributed to the simple fabrication process, an overall yield of 96% (24 out of 25 tested) of fully operational single filter stages was achieved. Fig. 3 shows a fabricated photonic filter with five cascaded unit cells that has been wire-bonded to a carrier for interfacing with two 14-pin multi connector probe-cards. The overall dimension of this device is  $4.5 \times 1.5$  mm. In order to avoid radiation loss from waveguide bends and keep the fabrication complexity to a minimum, deeply etched waveguides were used for the entire device; a cross section of the waveguide is shown in the inset of Fig. 3. For coupling, 3-dB restrictive multimode-interference (MMI) couplers, 100  $\mu\text{m}$  in length, were utilized everywhere, as shown in the inset of Fig. 3. The couplers have a measured total insertion loss of  $\sim 1.0$  dB/coupler. More details on the fabrication and integration platform have been published elsewhere [16].

## IV. EXPERIMENTS AND DISCUSSION

### A. Measurement Setup

In order to demonstrate the filtering function of our device, we characterize our filter in the optical as well as in the RF-electrical domain. The optical measurement is straight forward, as it only requires a broadband amplified spontaneous emission (ASE) spectrum input and an optical spectrum analyzer (OSA) to measure the output of the filter. The advantage of this technique is the wide bandwidth available, typically several tens of nm (several THz) using an erbium doped fiber amplifier (EDFA). Thus, this is useful for imaging more than one free spectral range (FSR) of our filter functions. However, the resolution of the OSA is limited to 0.01 nm (1.25 GHz), and will therefore not truthfully resolve the shape of any GHz

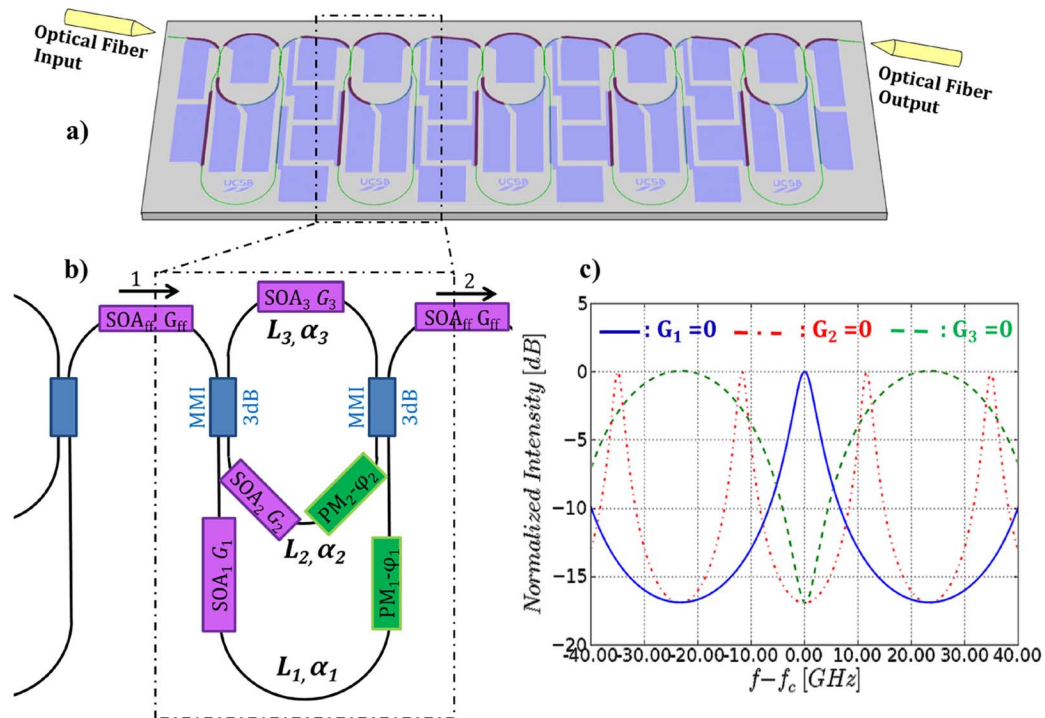


Fig. 2. (a) Illustration of programmable filter array chip. (b) A single filter stage and its functional components (SOAs, PMs and 3 dB MMI couplers) shown schematically. (c) Different filter responses generated by turning off different waveguide paths in the single filter stage ( $G_{1/2/3} = 0$ ), isolated pole and zero responses results.

wide filter shapes, especially not the ripple magnitudes in the passband.

In order to increase the resolution, but also to more closely mimic the real photonic microwave application, we use a heterodyne detection scheme to image the filter in the electrical RF-domain. A schematic of the measurement is shown in Fig. 4. In this measurement, a band limited noise spectrum is input to the device under test (DUT). This input simulates a wide bandwidth single sideband (SSB) modulated microwave signal that has been carrier suppressed. The noise spectrum is generated by an amplified spontaneous emission (ASE) source and is amplified by an EDFA before being sent through a circulator connected to a fiber Bragg grating (FBG) to produce the band limited input signal. In the heterodyne detection, the filtered signal is down converted using a tunable local oscillator (LO) laser, placed just to the side of the initial noise spectrum, as shown in the inset of Fig. 4. A 40 GHz photodiode (PD), with a 38 GHz broadband amplifier and a 50 GHz electrum spectrum analyzer (ESA) is used to image the output of the filter device. All data are normalized to the throughput (w/o DUT) in order to remove ripples originated from the FBG spectrum. The added receiver noise is measured by turning off the LO laser, and is subtracted from the measured data. The resolution of this RF electrical measurement is limited by the relative frequency stability of the LO laser and the DUT, over the time scale of the ESA frequency sweep. An upper bound on this resolution was established by comparing many subsequent measurements of the filter function. The maximum frequency deviation and hence worse resolution was found to be  $\sim 50$  MHz. The frequency drift is attributed to the DUT, as the frequency stability of the LO laser was characterized separately to  $\sim 10$  MHz. The total band-

width of the RF electrical measurement is about 35 GHz, limited by the electrical components. Thus, the optical and electrical RF measurements are good compliments to each other, being able to characterize the DUT in both high resolution and over a wide bandwidth. All measurements were done continuous wave (CW) at room temperature.

### B. Single Cell Filter Responses

We start by demonstrating the programmability of the single filter stage. The optical measurement was here used, to image a wide bandwidth and characterize the full frequency tunability. Also, for first order IIR and FIR filters there are no ripples or other details expected in the passband that would require the high-resolution measurement. However, we note that the measured stopband rejection for the MZI zero in Fig. 5(b) would possibly be slightly larger if a finer measurement resolution was used.

Fig. 5 demonstrates the reconfigurability and tunability of the single filter stage. In Fig. 5(a) the short resonator pole filter has been isolated by reverse biasing SOA<sub>1</sub> (see Fig. 2). By adjusting the currents on SOA<sub>2</sub> and SOA<sub>3</sub> the magnitude of the single pole is adjusted continuously. In order to keep the filter fixed in frequency (phase), the PM<sub>2</sub> is utilized to compensate for the parasitic phase shift induced by heating (positive added phase) and current injected (negative added phase), when changing the current on the SOAs. The pole-zero diagram of Fig. 5(a) shows the pole locations, as found by fitting the measured filter magnitude responses to (1). In Fig. 5(b) the arbitrary phase of the single filter stage is demonstrated using the MZI zero configuration.  $2\pi$  of tunability is achieved by utilizing only the phase modulator of one MZI arm. Tuning more than  $2\pi$  is never nec-

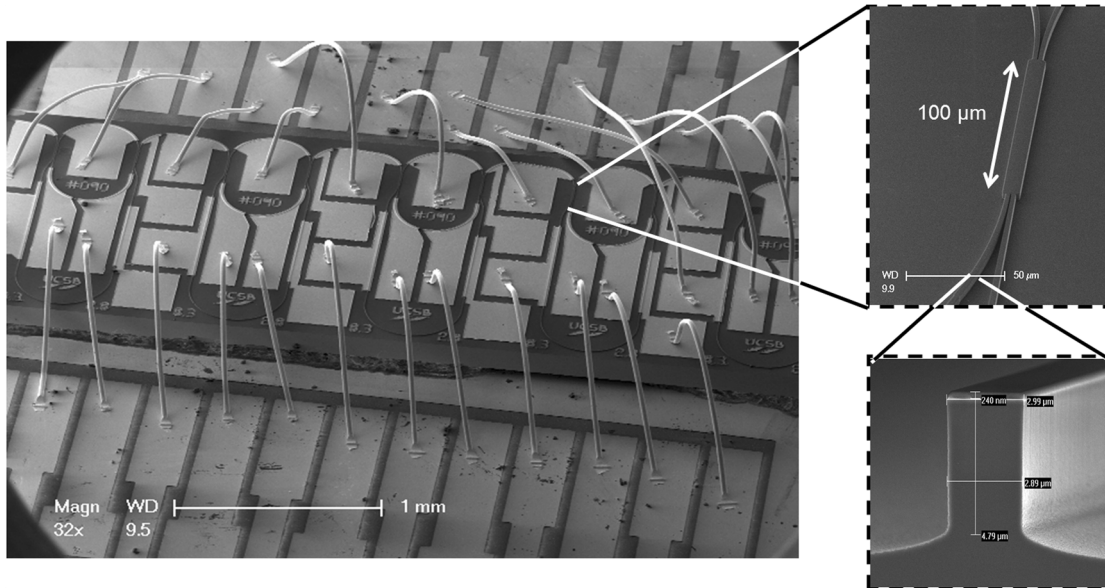


Fig. 3. Scanning electron microscopy (SEM) image of a programmable photonic filter device wire bonded to a carrier. Insets show deeply etched MMI coupler (upper) and a cross section of deeply etched waveguide (lower).

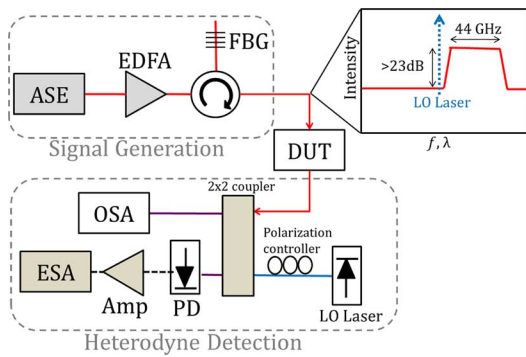


Fig. 4. Schematic illustration of the electrical RF-domain measurement setup.

essary, since this corresponds to the filter FSR where the pass-band is repeated. Although here showing  $\sim 47$  GHz of tunability, in reality the zero (and poles) can be placed anywhere in the SOA gain bandwidth (typically around 5 THz wide, i.e., the optical C-band).

We note that there is a slight ( $< 2$  dB) variation in stopband rejection as the zero is tuned around the unit circle (or over 47 GHz). This is due to the unbalancing of the MZI caused by the parasitic loss from free carrier absorption (FCA) when injecting current in the phase modulator, in only one of the MZI arms. This parasitic is easily compensated for by adjusting the SOA currents to balance the MZI path gains. However, to illustrate the point and quantify the magnitude of this parasitic, the SOA currents were kept unchanged in this demonstration.

In general, the pole and zero location can be tuned a full  $2\pi$ . However, the MZI zero magnitude is limited to about 0.77 (assuming minimum phase zero), or  $\sim 18$  dB of stopband rejection, as demonstrated in Fig. 5(b). The pole magnitude is not inherently limited in this fashion. But as the poles are tuned closer to the unit circle, the optical resonator approaches the lasing condition. This implies modal gain competition, which makes

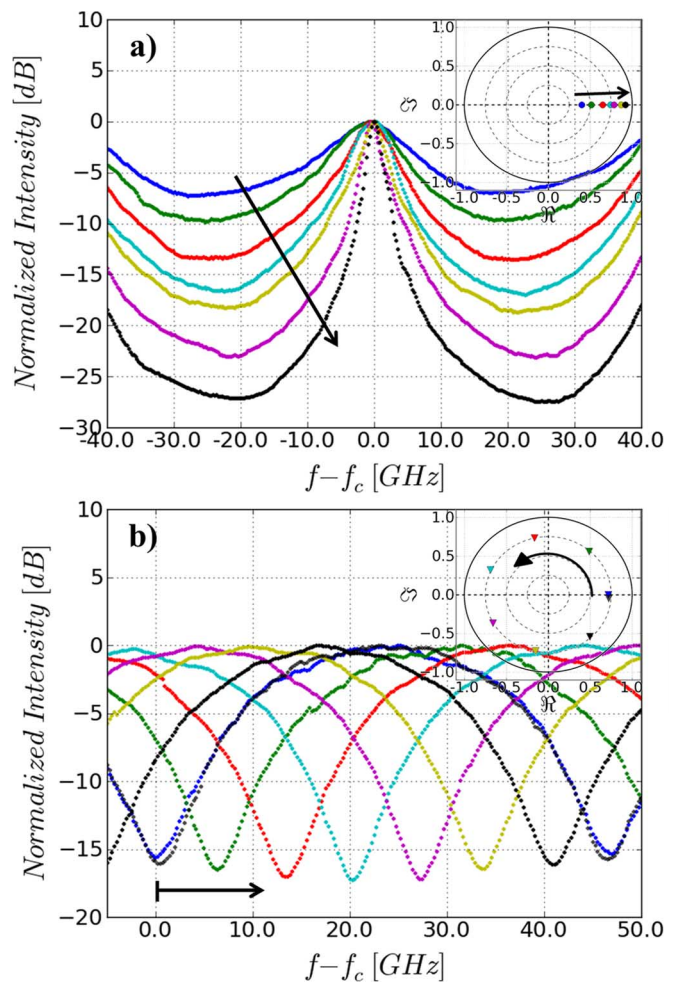


Fig. 5. Measured filter responses of a single filter stage reconfigured as a pole in (a) or zero in (b). Arbitrary placement of the pole/zero in the complex plane, demonstrated by independently adjusting the magnitude in (a) and phase in (b).

the filter synthesis non-linear, therefore compromising the linear filter synthesis and making the filter more difficult to control. In order to limit such negative effects, we decided to limit the pole magnitudes to  $<0.9$  when synthesizing higher order filters in this work.

### C. Higher Order Filters-Versatile Filter Synthesis

In order to demonstrate the versatile filter synthesis of our proposed cascaded filter structure, a variety of filter shapes are here demonstrated in Fig. 6. The filters are measured in the RF domain with higher resolution to accurately reveal the filter shapes, including quantifying in-band filter ripples. All filter responses have been centered at zero frequency for easy comparison. In the measurement the frequency offset between the filter center frequency and the LO ( $f_c - f_{LO}$ ) is typically around 20 GHz, in order to best image the full filter FSR. Simulations have been superimposed on the measured data (dashed curves in Fig. 6), and shows a good theoretical agreement with the ideal linear filter functions, described by (1)–(3). The pole and zero locations for each filter response are thereby also extracted.

Utilizing the minimum of two poles, a bandpass filter is created in Fig. 6(a). This filter was created with the long resonator delay and identical pole values of 0.73, a  $\sim 3.5$  GHz wide passband with 0.2 dB ripple and 23.5 GHz of filter FSR is demonstrated. By introducing an additional pole, larger stopband rejection and improved filter roll-off is achieved, as also shown Fig. 6(a). This third-order filter has a center pole magnitude of 0.74 with 0.83 magnitude poles on either side; the in-band ripple is 0.4 dB. Another way to improve rejection and roll-off is by introducing additional zeros instead of poles. This is illustrated in Fig. 6(b), where a total of four stages were utilized to create an elliptical filter with two poles and two zeros. The zeros are placed on either side of the passband. The  $\pi$  phase difference between the poles and zeros expected from the transfer functions (compare (5) and (6) and Fig. 2(c)), can also be seen in the pole-zero plot inset in Fig. 6(b).

The bandwidth over which the filter can operate is determined by the FSR, due to the repetition of the passband. For the longer resonator delay used to synthesize the filters in Fig. 6(a), (b), the FSR is 23.5 GHz. By using additional zeros, the FSR of the filters can be extended by placing zeros over neighboring passbands. This requires that the FSR of the zeros and poles are designed accordingly; in our single filter stage the FSR of the MZI zero is twice that of the long resonator delay (47 versus 23.5 GHz). In Fig. 6(c), two zeros are placed over the next filter order and thus enhancing the FSR from 23.5 to 47 GHz.

### D. Passband and Center Frequency Tunability

In the previous sections we have demonstrated the programmability of the single filter stage, and how several cascaded stages can provide versatile filter synthesis of higher order filters. In this section, we investigate general bandpass filters that have both bandwidth and center frequency tunability. These are the key filter functionalities desired for the optical signal processing in microwave photonic links, as was described in the introduction.

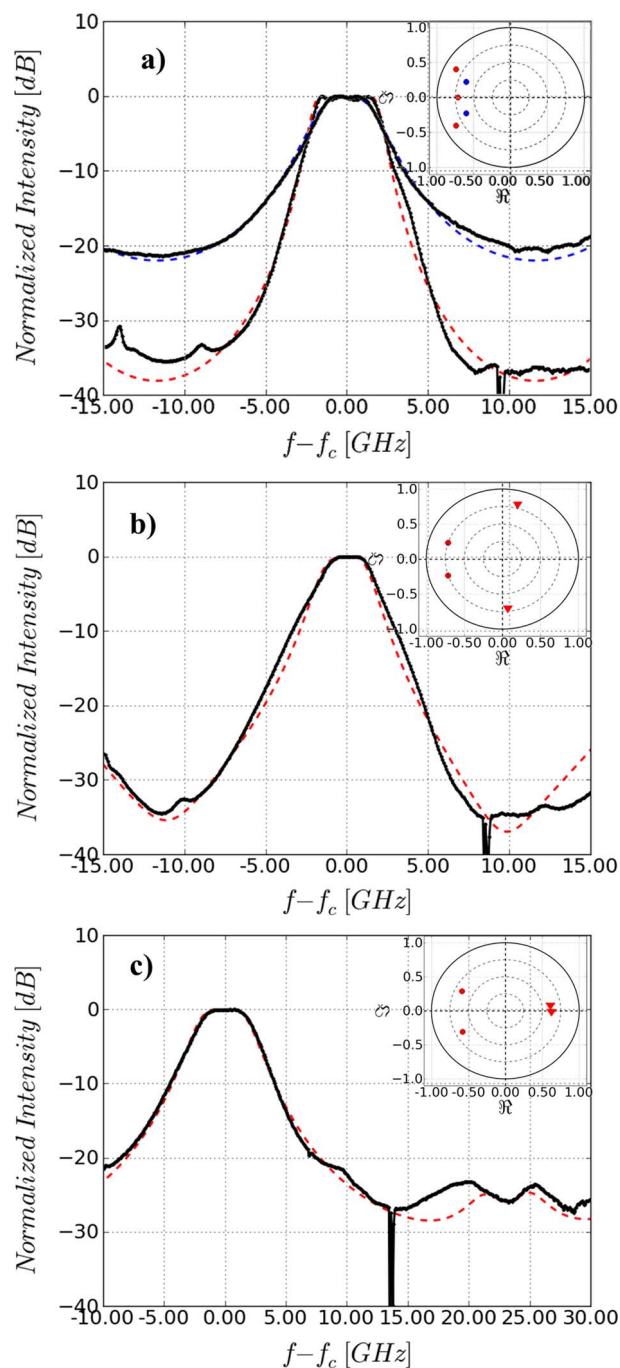


Fig. 6. Examples of higher order filters synthesized with our programmable filter device. Experimental data is represented with solid lines, theoretically fitted filter functions are superimposed with dashed lines. The fitted pole (circle) and zero (triangle) locations for each case are shown in the pole-zero diagram insets. The narrow notch feature evident in the experimental data (solid) is an artifact of the measurement, caused by a noise spike in the receiver resulting in the notch when the receiver noise is subtracted. (a) 2nd (red) and 3rd (blue) order bandpass filter using only poles. (b) Bandpass filter utilizing both zeros and poles. (c) 2nd order bandpass filter with zeros placed to eliminate the next filter order and thus double the FSR.

A family of filter functions have been programmed and superimposed in Figs. 7 and Fig. 8 to demonstrate the bandwidth and center frequency tuning capability of the filter device. The measured filter responses have again been fitted using (1)–(3) to find the pole locations. However, the actual simulation curves

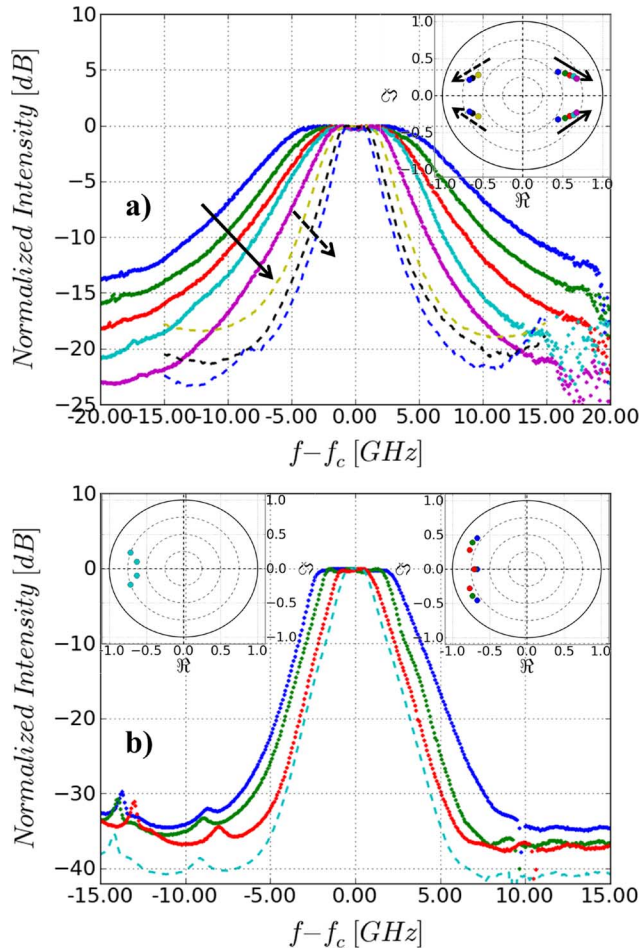


Fig. 7. (a) Bandwidth tunability for a 2nd order bandpass filter using the short (solid) and long (dashed) resonator. (b) Bandwidth tunability achieved with 3rd (dotted) and 4th order (dashed) bandpass filter.

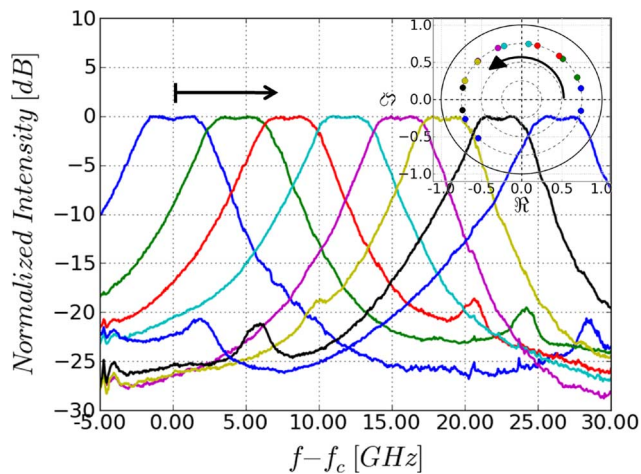


Fig. 8. Center frequency tunability demonstrated using a 2nd order bandpass filter.

have been left out from the figures to preserve the clarity of the measured filter responses.

Fig. 7(a) demonstrates the bandwidth tunability of a 2nd order bandpass filter, utilizing either the short or the long resonator

delay (solid and dashed line respectively). The passband tunability is achieved by introducing a phase difference between the poles that gives a desired bandwidth, and then adjusting the pole magnitude to get a preferred passband ripple; here, all ripples were kept  $< 0.3$  dB. The arrows in the pole-zero diagram of Fig. 7(a) show how the poles move in the complex plane when the bandwidth is tuned. A total 3 dB bandwidth tunability from 14 down to 3 GHz is here demonstrated while keeping the stopband rejection  $> 13$  dB. For the wider bandwidth filters, a low pole values must be utilized to achieve the flat passband; this unfortunately translates into slower filter roll-off and lower stop band rejection, as evident in Fig. 7(a). By introducing more filter stages (i.e., more zeros and/or poles), filter extinction and roll-off is improved. Fig. 7(b) shows the filter bandwidth tunability achieved using three (dotted) or four poles (dashed).

The stopband rejection is kept  $> 33$  dB, while the bandwidth is adjusted from 1.9–5.4 GHz. The polar plots of Fig. 7(b) display the pole arrangement of these higher order filters. It shows that these filters are neither a classical Butterworth nor a Chebyshev Type I filter [17], but rather a combination of the two. Fig. 7(b) also demonstrates the limit of measurable passband rejection in the experimental setup; the spurious peaks showing up in the stopband are caused by the measurement setup.

The second important functionality of a photonic filter is center frequency tunability. This should ideally be achieved without changing the filter shape. The frequency tuning of our filter is achieved by tuning the individual poles and zeros (i.e., filter stages) by the same amount. Thus, every filter response demonstrated previously, can also be arbitrarily tuned in center frequency. Fig. 8 demonstrates the frequency tunability using a second order bandpass filter, where the shorter resonator delay is utilized. The filter shape is kept roughly constant with a passband bandwidth of  $\sim 5$  GHz, while the center frequency is tuned from 0 to 27 GHz. The pole plot shows how the poles are tuned as a pair in the unit circle with a fixed phase difference and constant pole values of 0.75. The filter can be tuned a full 48 GHz ( $2\pi$ ), but the tuning bandwidth is here limited by the measurement bandwidth to image the filter responses. We note that in a real application, the filtering domain is really  $f_c - f_{lo}$  to  $f_c - f_{lo} + 48$  GHz, based on the heterodyning receiver scheme. In this experiment,  $f_c - f_{lo} = 10$  GHz, thus the filtering domain was in fact 10–58 GHz. This ability of signal filtering at arbitrary frequencies is a quality of photonic filtering unmatched in electronics.

### E. Filter Linearity

For many real system applications, the requirement of a linear signal transfer function is very crucial. For microwave applications this is characterized by the spurious-free dynamic range (SFDR). Typical microwave applications, including radar, desire SFDR numbers in the range  $105$ – $120$  dB $\cdot$ Hz $^{2/3}$  [18], [19]. A strength of our active filter device is the ability to compensate for inherent signal loss that would otherwise yield very large noise figures (NF) and degrade the SFDR. However, there is also a drawback in using active semiconductor material, in the introduction of excess noise and the potentially non-linear gain.

The noise figure is easily quantified by measuring the output spontaneous emission spectral density ( $S_{sp}$ ) together with the signal gain ( $G$ ). The NF is given by [20]:

$$NF = \frac{2S_{sp}}{h\nu G} + \frac{1}{G} \quad (7)$$

where the first term corresponds to the ASE noise and the second term is the enhancement in shot noise. The electrical noise current generated in the heterodyne detection, assuming ideal shot noise limited detection, is then given by

$$i_{noise} = \sqrt{2qR(P_{out} + P_{LO})NF} \quad (8)$$

$P_{out}$  is the optical power output from the filter (signal together with the generated ASE noise power) and  $P_{LO}$  is the power of the LO.

The filter non-linearity can be characterized by passing two laser tones through the filter passband and examining the generated four-wave mixing (FWM) intermodulation distortion (IMD) terms. By varying the input laser power and recording the power in the fundamental and the third order intermodulation distortion (IMD3) terms, an equivalent optical output third order interception point (OIP3) is found. Again, the optical power is converted to an electrical current in the heterodyne detection scheme according to

$$i_{OIP3} = \sqrt{P_{OIP3}P_{LO}}R. \quad (9)$$

Utilizing a strong LO,  $P_{LO} \gg P_{in}$  (in our measurement  $P_{LO} = 10$  dBm  $\gg P_{out} = -10$  dBm), the LO power cancels out in the expression for the SFDR

$$SFDR = \left( \frac{i_{OIP3}^2}{i_{noise}^2} \right)^{2/3} \approx \left( \frac{P_{OIP3}R}{2qNF} \right)^{2/3}. \quad (10)$$

This approach of characterizing the non-linearity of an optical device using two laser tones w/o modulators, has been investigated before [21], [22]. Compared to the more conventional approach of producing the input optical tones using optical modulators [23], this measurement eliminates the possibility of non-linearities originated from the optical modulators and being amplified in the SOAs [22].

We have characterized the SFDR of a two-stage filter device, while synthesizing a bandpass filter similar to those shown in Fig. 7. Two stable DFB lasers were used as the fundamental input tones, and were spaced by 110 MHz. In order to resolve the fundamental and generated IMD tones, the same receiver setup as in Fig. 4 was utilized, but without the electrical amplifier. The DC optical power was kept constant in the measurement by applying a third laser input to the filter, spaced far away from the two DFB lasers to avoid FWM with this laser. The OIP3 of the receiver (PD and ESA) was measured to be  $>30$  dBm. A down converted filter output is shown in the inset of Fig. 9. Fig. 9 plots the powers of the fundamental and third order intermodulation tones versus the fundamental tone. The data is fitted to lines with slopes of 1 and 3 as predicted by theory; from this an extrapolated optical OIP3 point of  $-3.2$  dBm is established.

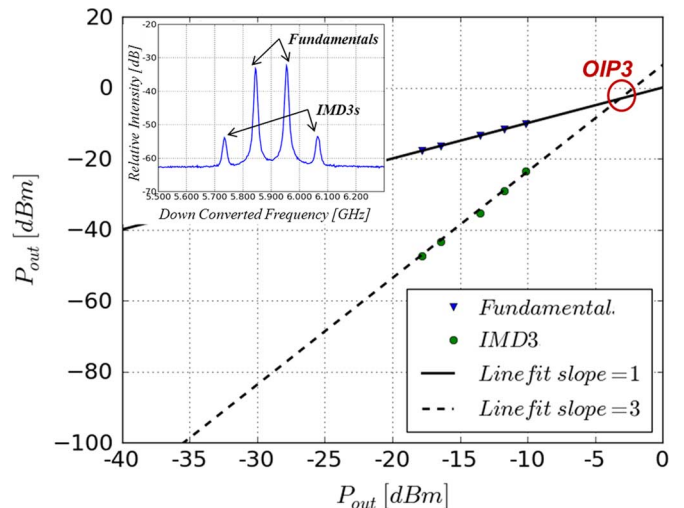


Fig. 9. Measured optical OIP3 for our active photonic filter structure. Inset shows a spectrum with the fundamental and generated IMD3 tones.

The NF was measured to be 23.2 dB, yielding an SFDR of  $86.3$  dB\* Hz $^{2/3}$ .

We believe that the SFDR number established here can be significantly improved upon, mostly by redesigning the amount of gain in the filter. In the current device design, there is a large overdesign in gain with around 16 dB excess gain in each resonator. Thus, the SOAs are currently biased close to transparency where they are very nonlinear and have worse NFs [15], [19]. Also by optimizing the actual SOA epitaxial design the linearity will improve significantly. The current SOA design have a maximum 3-dB saturation power ( $P_s$ ) of 11.4 dBm, while we have previously demonstrated SOAs with  $P_s > 20$  dBm on a similar integration platform [24], where the OIP3 scales with  $P_s^2$  [21]. It is expected that scaling to more filter stages will not produce much worse NFs (and SFDR), since, when cascading amplifiers the overall NF can be limited if the gain is distributed correctly, similar to cascaded electronic amplifiers [20].

## V. CONCLUSION AND FUTURE DIRECTION

We have investigated a novel programmable photonic filter architecture, consisting of an array of identical filter stages, each capable of producing a single zero or pole. We first demonstrated the reconfigurability of the single filter stage and the ability to arbitrarily place zeros and poles in the complex plane. Next, versatile filter synthesis of various higher order filters was presented. Finally, we demonstrated a bandpass filter with tunable passband bandwidth of from 1.9–14 GHz, and center frequency over 27 GHz. Such filter characteristics could be valuable for real analog signal processing applications of wide bandwidth signals. For many RF-applications however, a sub-GHz filter is ultimately desired. The lower limit on passband bandwidth presented in this paper (1.9 GHz) is inherent to the resonator delays. In the future, the bandwidth could be narrowed, simply by making longer delays.

In this work, a total of five cascaded filter stages were monolithically cascaded, however, so far a maximum of four stages has simultaneously been utilized to synthesize filters. This



is attributed to the limited number of current/voltage control sources available in the testing setup and the complexity of manual control. Future work will include interfacing the filter with a computer or a field programmable gate array (FPGA). This will allow us to scale to larger filter structures and improve the ease of filter synthesis and control. We investigated the linearity of our active filter design, with a resulting SFDR of  $86 \text{ dB} \cdot \text{Hz}^{2/3}$ . This is unfortunately not enough for most practical RF-system applications, but we are confident that this number can be greatly improved by re-designing the amount of gain in the device and utilizing a more linear SOA epitaxial design. Hence, investigating the scalability and control together with improving the linearity of our filters is the focus of current research.

## REFERENCES

- [1] T. Kun-Yii, M. S. Rasras, D. M. Gill, S. S. Patel, C. Young-Kai, A. E. White, A. Pomerene, D. Carothers, J. Beattie, M. Beals, J. Michel, and L. C. Kimmerling, "Silicon RF-photonic filter and down-converter," *J. Lightw. Technol.*, vol. 28, no. 20, pp. 3019–3028, Oct. 2010.
- [2] J. Campany, B. Ortega, and D. Pastor, "A tutorial on microwave photonic filters," *J. Lightw. Technol.*, vol. 24, no. 1, pp. 201–229, Jan. 2006.
- [3] J. E. Bowers, S. A. Newton, W. V. Sorin, and H. J. Shaw, "Filter response of single-mode fibre recirculating delay lines," *Electron. Lett.*, vol. 18, no. 3, p. 110, Feb. 1982.
- [4] A. Agarwal *et al.*, "Fully programmable ring-resonator-based integrated photonic circuit for phase coherent applications," *J. Lightw. Technol.*, vol. 24, no. 1, pp. 77–87, Jan. 2006.
- [5] Y. Ma, S. Chang, S. Chang, and S. Ho, "Improved optical filter responses in cascaded InGaAsP/InP microdisk resonators," *Electron. Lett.*, vol. 37, no. 9, pp. 564–565, Apr. 2001.
- [6] E. J. Norberg, R. S. Guzzon, S. C. Nicholes, J. S. Parker, and L. A. Coldren, "Programmable photonic lattice filters in InGaAsP-InP," *Photon. Technol. Lett.*, vol. 22, no. 2, pp. 109–111, Jan. 2010.
- [7] P. Toliver *et al.*, "A programmable optical filter unit cell element for high resolution RF signal processing in silicon photonics," in *Proc. OFC/NFOEC*, San Diego, CA, 2010, pp. 1–3, Paper OWJ4.
- [8] S. Ibrahim *et al.*, "Fully reconfigurable silicon photonic lattice filters with four cascaded unit cells," in *Proc. OFC/NFOEC*, San Diego, CA, 2010, pp. 1–3.
- [9] H.-W. Chen, A. W. Fang, J. Bovington, J. Peters, and J. Bowers, "Hybrid silicon tunable filter based on a Mach-Zehnder interferometer and ring resonator," in *Proc. Microw. Photon.*, Valencia, Spain, 2009, pp. 1–4.
- [10] R. S. Guzzon, E. J. Norberg, J. S. Parker, L. A. Johansson, and L. A. Coldren, "Monolithically integrated programmable photonic microwave filter with tunable inter-ring coupling," in *Proc. Microw. Photon.*, Montreal, QC, Canada, 2010, pp. 23–26.
- [11] E. J. Norberg, R. S. Guzzon, J. S. Parker, L. A. Johansson, and L. A. Coldren, "A monolithic programmable optical filter for RF-signal processing," in *Proc. Microw. Photon.*, Montreal, QC, Canada, 2010, pp. 365–368.
- [12] E. J. Norberg, R. S. Guzzon, J. S. Parker, and L. A. Coldren, "Programmable photonic filters from monolithically cascaded filter stages," in *Proc. Integrated Photonics Research, Silicon and Nanophotonics*, Monterey, CA, 2010, ITuC3.
- [13] C. K. Madsen and J. H. Zhao, *Optical Filter Design and Analysis: A Signal Processing Approach*. Hoboken, NJ: Wiley-Interscience, ch. 6.
- [14] L. A. Coldren and S. W. Corzine, *Diode Lasers and Photonics Integrated Circuits*. Hoboken, NJ: Wiley-Interscience, 1995, p. 218.
- [15] L. A. Coldren and S. W. Corzine, *Diode Lasers and Photonics Integrated Circuits*. Hoboken, NJ: Wiley-Interscience, 1995, p. 360.
- [16] E. J. Norberg, R. S. Guzzon, S. C. Nicholes, J. S. Parker, and L. A. Coldren, "Programmable photonic filters fabricated with deeply etched waveguides," in *Proc. Indium Phosphide Related Materials*, Newport Beach, CA, 2009, pp. 163–166.
- [17] C. K. Madsen and J. H. Zhao, *Optical Filter Design and Analysis: A Signal Processing Approach*. Hoboken, NJ: Wiley-Interscience, pp. 142–149.
- [18] S. A. Pappert and B. Krantz, "RF photonics for radar front-ends," in *Proc. IEEE Radar Conf.*, Boston, MA, 2007, pp. 965–970.
- [19] P. Berger, J. Bourderionnet, M. Alouini, F. Bretenaker, and D. Dolfi, "Theoretical study of spurious-free dynamic range on a tunable delay line based on slow light in SOA," *Opt. Exp.*, vol. 17, no. 22, pp. 20584–20597, 2009.
- [20] D. M. Baney, P. Gallion, and R. S. Tucker, "Theory and measurement techniques for the noise figure of optical amplifiers," *Opt. Fiber Technol.*, vol. 6, pp. 122–154, 2000.
- [21] Y. C. Chung, J. M. Wiesenfeld, G. Raybon, and U. Koren, "Intermodulation distortion in a multiple-quantum-well semiconductor optical amplifier," *Photon. Technol. Lett.*, vol. 3, no. 2, Feb. 1991.
- [22] R. D. Esman and K. J. Williams, "Measurement of harmonic distortion in microwave photodetectors," *IEEE Photon. Technol. Lett.*, vol. 2, no. 7, pp. 502–504, Jul. 1990.
- [23] T. Ohno, H. Fukano, Y. Muramoto, T. Ishibashi, T. Yoshimatsu, and Y. Doi, "Measurement of intermodulation distortion in a unidirectional refracting-facet photodiode and a p-i-n refracting-facet photodiode," *IEEE Photon. Technol. Lett.*, vol. 14, no. 3, pp. 375–377, 2002.
- [24] J. Raring, E. Skogen, M. Mašanovic, S. DenBaars, and L. Coldren, "Demonstration of high saturation power/high gain SOAs using quantum well intermixing and MOCVD regrowth," *IEE Electron. Letts.*, vol. 41, pp. 1345–1346, Nov. 2005.

**Authors' biographies not included at authors request due to space constraints.**